# Polymorphism Complexity and Handedness Inversion in Serum Albumin Amyloid Fibrils

Ivan Usov, Jozef Adamcik, and Raffaele Mezzenga*

Food & Soft Materials Science, Department of Health Science & Technology, ETH Zurich, Schmelzbergstrasse 9, LFO E23, 8092 Zurich, Switzerland

ABSTRACT Protein-based amyloid fibrils can show a great variety of polymorphic structures within the same protein precursor, although the origins of these structural homologues remain poorly understood. In this work we investigate the fibrillation of bovine serum albumin—a model globular protein—and we follow the polymorphic evolution by a statistical analysis of high-resolution atomic force microscopy images, complemented, at larger length scales, by concepts based on polymer physics formalism. We identify six distinct classes of coexisting amyloid fibrils, including flexible left-handed twisted ribbons, rigid right-handed helical ribbons and nanotubes. We show that the rigid fibrils originate from flexible fibrils through two diverse polymorphic transitions, first, via a single-fibril transformation when the flexible left-handed twisted ribbons turn into the helical left-handed ribbons, to finally evolve into nanotube-like structures, and second, via a double-fibril transformation when two flexible left-handed twisted ribbons wind together resulting in a right-handed twisted ribbon, followed by a rigid right-handed helical ribbon polymorphic conformation. Hence, the change in handedness occurs with an increase in the level of the fibril's structural organization.

Handedness inversion
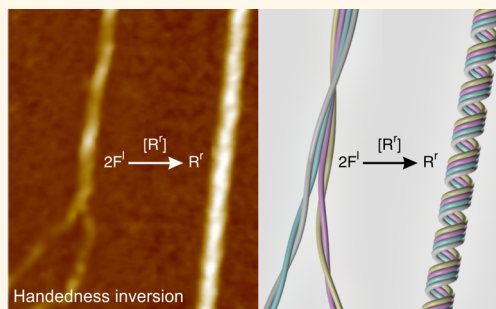
KEYWORDS: bovine serum albumin · protein self-assembly · amyloid fibrils · statistical analysis · polymorphism · handedness · atomic force microscopy

The field of globular protein fibrillation has gone through a rapid development over the last decades. It was found that the formation of fibrillar arrangements is driven by several noncovalent intermolecular forces, including hydrophobic and electrostatic interactions, ionic and hydrogen bonding, and van der Waals attraction.[1−3] The resulting quaternary structures of proteins or polypeptides, the so-called amyloid fibrils, are mainly characterized by well-defined cross-β-sheet layering perpendicular to a fibril's main axis.[4,5] There is a broad range of proteins reported being able to arrange in such a way. *In vivo*, this self-assembly scheme occurs for fibroin in spider silk fibers,[6] and it is also preeminent in neurodegenerative disorders, such as Parkinson's, Alzheimer's, and diabetes mellitus type II,[7,8] where insoluble amyloid fibrils accumulate in the extracellular space of various tissues and organs, disrupting their proper functionality.[9−11] *In vitro*, many food-grade proteins, such as α-lactalbumin,[12,13] β-lactoglobulin,[12,14−16] ovalbumin,[17,18] and lysozyme,[19−21] can also form amyloid fibrils under appropriate treatment. Depending on incubation conditions (pH, temperature, ionic strength, protein concentration, incubation time, presence of denaturation surfactants, *etc.*), the structures obtained can range from random aggregates to flexible, semiflexible, and rod-like objects. These fibrils have a potential application as functional food ingredients such as texture builders and foaming or gelling agents.[22−24] Furthermore, due to their high strength and elasticity, amyloid fibrils can be used as templates for a variety of biomaterials and advanced devices.[25−27] Hence, protein self-assembly is an important process and of great relevance in many different scientific areas, among them biomedical research, food science, nanotechnology, and biomaterials science.

It has been reported previously that the globular protein bovine serum albumin (BSA) can aggregate or fibrillate into β-sheet-rich structures under a broad range of incubation conditions.[28−34] In most of

the cases, self-assembly was achieved by applying high temperatures (60−80 °C), with different salt concentrations (0−300 mM), and in a wide window of pHs (from 2 to 7.5). Randomly aggregated proteins or short flexible fibrillar structures with increased intermolecular β-sheet content and evidence of α-helices denaturation were reported, bearing evidence for amyloid formation. In this study the conditions within which BSA fibrillation is performed were chosen to be similar to those previously followed for β-lactoglobulin,[35] ovalbumin,[17] and lysozyme[19] fibril formation (90 °C and pH 2) but at higher protein concentration (6 w/w % BSA protein solution).

The BSA fibrillar structures assembled during the fibrillation process were characterized in detail using atomic force microscopy (AFM), revealing details of the structure at the single fibril length scale.[14,15,36,37] The XYZ coordinates of the fibrils' middle lines were extracted from AFM images *via* an in-house-developed processing and tracking software. Thus, basic morphological parameters such as total contour length, average height, or pitch size could be evaluated from a systematic statistical analysis performed on the extracted coordinates, in analogy with previous work from our group on other classes of amyloids.[14,35] Moreover, by applying polymer physics concepts on the tracked coordinates of the fibrils,[14,19,36] larger length scale structural information such as persistence length and scaling exponent were also determined, providing valuable information on the structural identification and characterization.

The results from such analysis show some surprising findings. We found that, at the beginning of the fibrillation process, BSA assembles into flexible fibrils with left-handed twisted ribbon morphology, while upon increasing the incubation time, the existence of the rigid fibrils starts to be observed. These rigid fibrils can originate from the flexible fibrils following two different pathways of polymorphic transitions: a single-fibril and a double-fibril transformation pathway, respectively. The single-fibril pathway is the transformation of the flexible left-handed twisted ribbons into left-handed helical ribbons, finally closing into nanotube-like structures. In the case of the double-fibril pathway, two flexible left-handed twisted ribbons wind together into a right-handed twisted ribbon, followed by the formation of a rigid right-handed helical ribbon. Thus, the coexistence of left- and right-handed fibrils self-assembled from the same globular protein is unambiguously identified, and the individual polymorphic transient intermediates were fully resolved.

RESULTS AND DISCUSSION

BSA Assembles into Different Amyloid Structures during the Fibrillation Process. Figure 1A illustrates AFM snapshots of the samples acquired at given incubation times, 6, 40, 70, 100, and 145 h, when the BSA solution was incubated at 90 °C and pH 2. At these conditions, the native state of the protein undergoes not only denaturation but also hydrolysis, similarly to what was reported in other globular protein systems such as β-lactoglobulin, lysozyme, and ovalbumin.[17,35,38] Sodium dodecyl sulfate polyacrylamide gel electrophoresis (SDS-PAGE) analysis displays a decrease in molecular weight from a single BSA molecule mass of 66 kDa to relatively small polypeptide masses below 6.5 kDa in the first 40 h (Figure S1). Circular dichroism (CD) measurements of the filtered samples were performed in order to confirm the amyloid nature of the BSA fibrils. CD spectra show β-sheet-rich content at 40 and 100 h of incubation, represented by a pronounced peak around the wavelength value 217 nm (Figure S2). The first class of relatively short and flexible fibrils starts to appear at 6 h. Upon further incubation their length and number monotonically grow up to 40 h, which results in an increase of the coverage area of AFM substrates by the fibrils. Between 40 and 70 h of incubation a new class of rigid fibrils originates and coexists with the flexible fibrils for the remaining incubation. Flexible BSA fibrils with similar shape visualized by transmission electron microscopy have been previously reported after fibrillation processes at 60 °C, pH 2, 0.2−0.3 M salt, 10 h[30] and 70 °C, pH 7.4, no salt, 96 h.[28] However, to date, rigid BSA fibrils have never been detected. The coexistence of flexible and rigid fibrils has also been reported for ovalbumin[17] and for β-lactoglobulin incubated in an ethanol−water mixture.[35] For 100 and 145 h samples it is possible to observe that the coverage area of the substrate by both fibril classes progressively decreases. Inset photographs of the solutions within the sample tubes show an increase of the brownish color over time. The solution becomes more viscous, as it can clearly be seen by the presence of trapped bubbles after 145 h of incubation (Figure 1A, 145 h, inset). These are indications that grown to a certain length, BSA fibrils start to entangle and form aggregates upon stirring. The presence of aggregates at later stages of incubation is also confirmed by AFM (Figure S3).

Within the broad diversity of BSA fibrils, two subclasses of flexible and four subclasses of rigid fibrils can be distinguished (Figure 1B). Figure 1C represents the longitudinal height profiles of the fibrils displayed in Figure 1B, by which six types of fibrils can be determined. Within the class of flexible fibrils there are thin fibrils with a visible periodical change in height along the contour (cyan) and thick fibrils with a random height fluctuation profile (violet). Rigid fibrils have four different morphologies: thin without periodicity (green), thin with periodicity (red), thick without periodicity (orange), and thick with periodicity (blue). Figure 1D displays the chronological appearance of the different fibril subclasses in the solution.

Detailed Morphology of the BSA Fibrils and Fibril Tracking Procedure. We have detected six different types of the
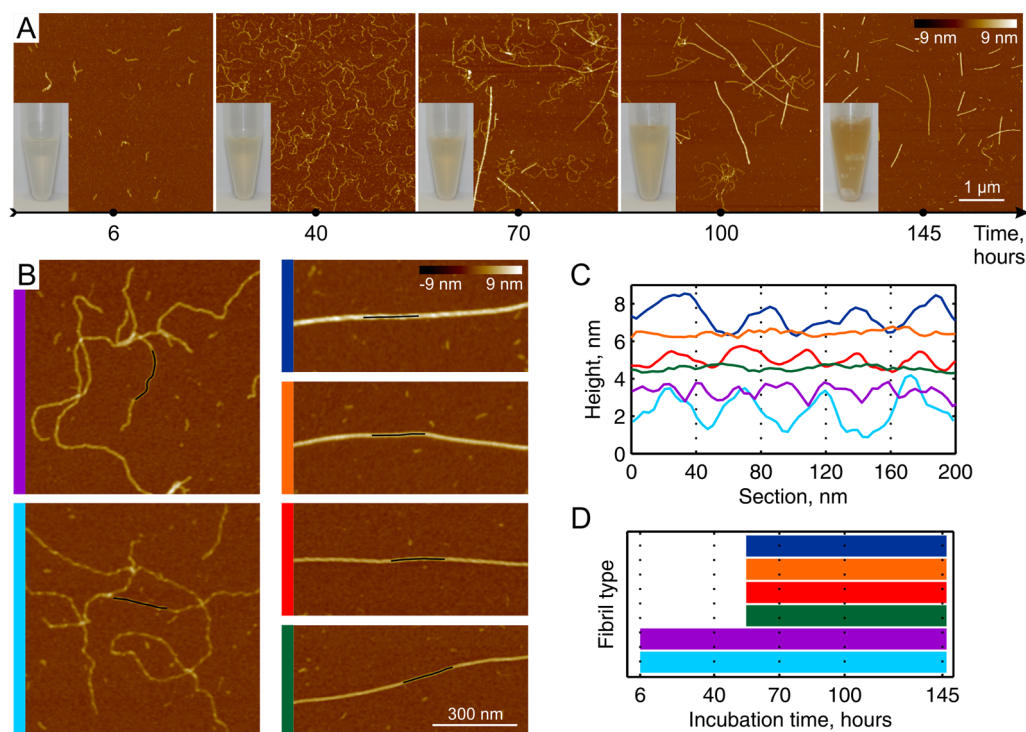
Figure 1. (A) AFM snapshots of the 6 w/w % BSA solution incubated at 90 °C and pH 2 after different incubation times (left to right: 6, 40, 70, 100, and 145 h). In preparation of the AFM samples, the solution was diluted to 0.1 w/w % protein concentration prior to deposition on mica. Inset images show the visual appearance of the corresponding samples. (B) AFM images of the different types of the BSA fibrils: thick flexible with random height fluctuations (violet), thin flexible with periodicity (cyan), thick rigid with periodicity (blue), thick rigid without periodicity (orange), thin rigid with periodicity (red), thin rigid without periodicity (green). Black lines are longitudinal sections of the fibrils with their height profiles displayed in panel (C). (D) Chronological appearance of each fibril type. Color codes are used consistently to identify fibril types in panels (B), (C), and (D).

BSA fibrils based on their average height and presence of periodical structure along their contour length. In order to characterize them in detail, we performed high-resolution AFM imaging and built 3D schematic representations based on them (Figure 2A−C). Magnified AFM images show that two types of rigid fibrils with cylindrical-like shape possess no visible periodicity along their contours (Figure 2A). Rigid fibrils with periodicity have a conformation of right-handed helical ribbons (Figure 2B). Finally, flexible fibrils can be described as left-handed twisted ribbons composed of two protofilaments (Figure 2C). The fact that flexible thin fibrils have clearly visible height fluctuations while flexible thick ones do not, may indicate that only in the first case is the cross section of the fibril sufficiently far from being axiosymmetric, whereas in the second case the maximum and minimum height should be much closer. This last scenario, in multistranded fibrils, can, in principle, be realized *via* a noncylindrical cross section of the composing protofilaments.[39] For the sake of simplicity, when building the 3D schematic representations, we used a simple cylindrical shape for the individual protofilaments in each of the two flexible fibril types. Figure S4 shows the occasional presence of relatively long protofilaments adsorbed on mica in a free state, as well as the presence of short fragments in the background.

In order to easily identify the polymorphic states, next we use the following notation: the main symbol F stands for flexible and R for rigid. A subscript represents the thickness of a fibril: 1 for thin and 2 for thick fibrils. A superscript displays the handedness of an object: l is left handed, r is right handed, and 0 is absence of observable handedness. Thus, the BSA fibril nomenclature is F_1^l for flexible thin left-handed (cyan), F_2^l for flexible thick left-handed (violet), R_1^0 for rigid thin without handedness (green), R_2^0 for rigid thick without handedness (orange), R_1^r for rigid thin right-handed (red), and R_2^r for rigid thick right-handed (blue) (see Figure 2A−C). Figure 2D illustrates the basics of the fibril coordinates' acquisition procedure. Each tracked fibril is characterized by its contour: a sequence of points ordered along the fibril's middle line from one end to the other (Figure 2D, top). All contours have a constant distance between the point's projections on the XY plane, the step size s, which has a typical value of about the pixel size of the AFM image (Figure 2D, bottom). Thus, the coordinates x_i, y_i (in the image plane) and z_i (height) of all the points incorporated by the contour provide a complete spatial description of the fibril middle line. All coordinates extracted in this way were further used in a statistical analysis. More details about the fibril tracking process are given in the Materials and Methods.
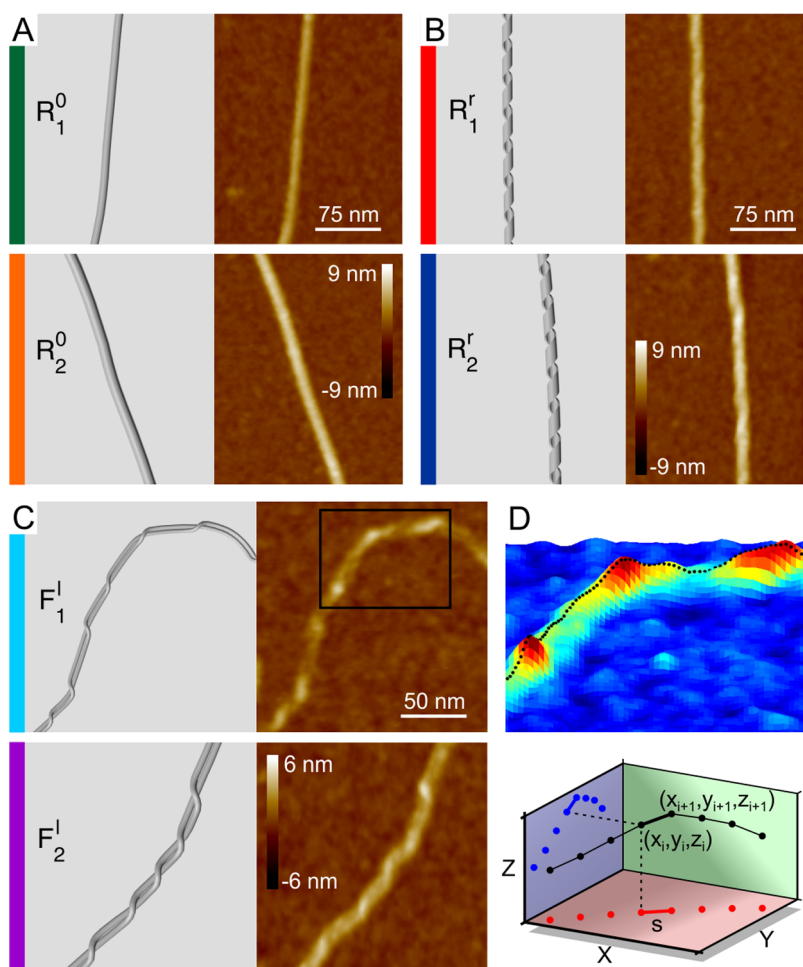
Figure 2. Magnified AFM images and their 3D schematic representations of (A) rigid nanotube-like fibrils without periodicity, type R_1^0 (top) and type R_2^0 (bottom); (B) rigid helical ribbon fibrils with periodicity, type R_1^r (top) and R_2^r (bottom); (C) flexible thin F_1^l (top) and flexible thick F_2^l (bottom) twisted ribbon fibrils. Color codes are used to identify fibril types consistently. (D) AFM 3D map of the selected region from (C) with black spots indicating positions of the contour points along the middle line of the fibril (top). Graphical illustration of the contour ensemble, where each point has three spatial Cartesian coordinates separated by a constant distance s in the image plane XY (bottom).

Statistical Analysis of the BSA Fibrils. Coordinates of fibrils extracted in the tracking process (Figure 2D) were further used for a systematic statistical analysis. Figure 3A−C depict fibril average height histograms for each fibril type, and Figure 3D shows the summary. All results for statistical analysis of the height values are explained in the Supporting Information (SI) and collected in Table S1. Pitch size estimation for the fibril subclasses with height periodicity was performed by fast Fourier transform (FFT) analysis of the height profiles. An FFT is an algorithm used to calculate the Fourier transform of discrete functions (DFT):

$$A_k = \sum_{n=1}^{N} h_n e^{-2\pi i(k-1)(n-1/N)} \qquad (1)$$

$$k = 1, ..., N$$

where h_n is the height of the nth point, N is taken as a maximal number of points in a contour among tracked fibrils of a certain subclass, and i is the imaginary unit. Amplitude A_k of the DFT describes the presence of a frequency component k in a height profile. Prior to calculation the first-order polynomial line was subtracted from each fibril profile to center the average height value at zero. Obtained FFT curves were then averaged using fibril lengths as weight factors. Figure 3E,F show resulting Fourier transforms for fibril types F_1^l and R_1^r, which are rescaled for the 1 μm length. Peaks related to the fibril periodicity in each case are marked with colored stripes. Hence, from the inverse of the dominating frequency, the fibril periodicity p is found to be 40−50 nm for F_1^l and 35−40 nm for R_1^r as well as R_2^r (Figure S6).

In order to analyze the period of twisted/helical ribbons and their morphology in more detail, the autocorrelation function R_{xx} was implemented on the height h, as well as on angular twist θ of the fibrils. The discrete autocorrelation function has the following form:

$$R_{xx}(m) = \frac{1}{N-m} \sum_{n=0}^{N-1-m} x_n x_{n+m} \qquad (2)$$
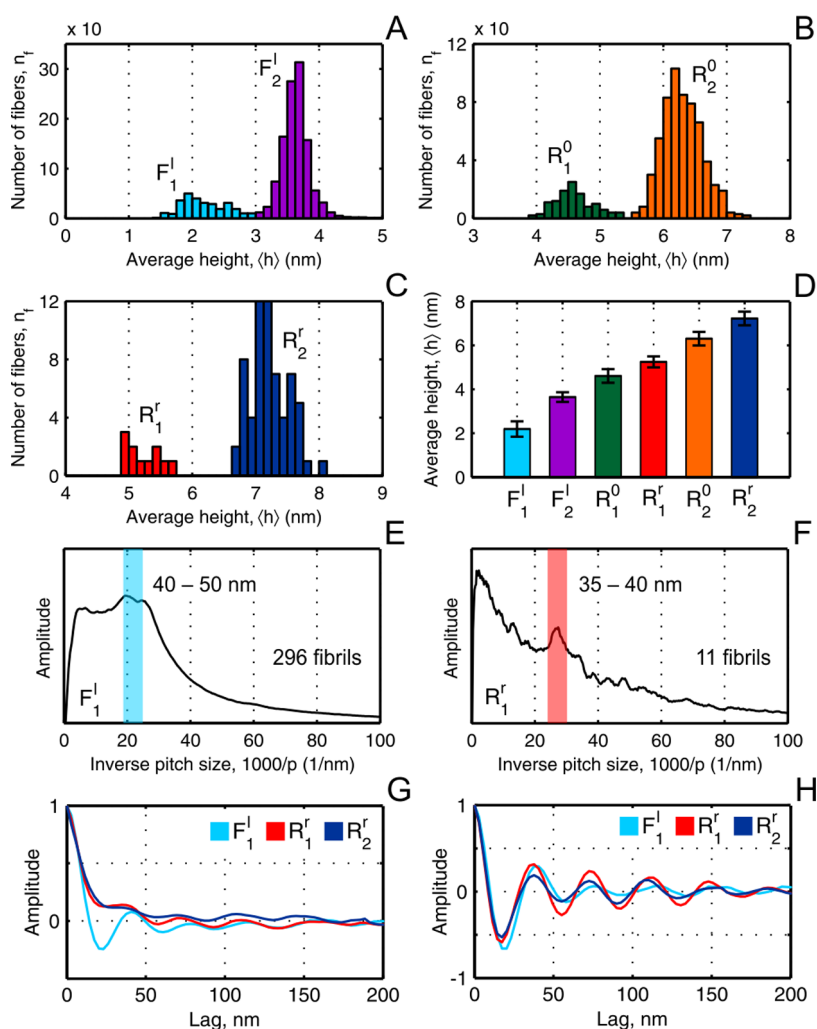
Figure 3. Average height distributions of (A) types F_1^l and F_2^l, (B) types R_1^0 and R_2^0, and (C) types R_1^r and R_2^r. (D) Bar chart of the sorted subclass average height $\langle H \rangle$ values (exact numbers are collected in Table S1). Pitch size estimation based on DFT of the height profiles for the types F_1^l (E) and R_1^r (F). Colored stripes cover peaks related to the fibril averaged pitch sizes. Averaged autocorrelation functions of the height (G) and the twisted/helix angle profiles (H) along the fibril middle lines.

where N is the total number of points along a fibril contour, m is a lag distance, and x identifies the discrete function of interest (h_n or θ_n in our case). Similar to the case of FFT analysis, all height profiles were centered at zero prior to use. The twist/helix angular data were obtained through the maxima and minima height peak positions. The final averaging between all fibrils is weighted according to their total lengths. Figure 3G, H show the resulting curves for fibril types F_1^l, R_1^r, and R_2^r. The mainly positive height autocorrelation amplitude values (Figure 3G) identify helical ribbon conformation for the rigid types, while the twisted ribbons F_1^l also possess correlations with a negative amplitude. This observation further comfirms our earlier discussion on the morphological shapes of the periodical fibrils. Both autocorrelation functions provide an alternative way to extract the period p of the fibrils, which is identical and consistent with that obtained by the DFT method: 41 nm for F_1^l and 38 nm for both R_1^r and R_2^r. Therefore, the autocorrelation

function is a powerful way to identify both periodicity and topology of fibrils.

The persistence length (λ) is one of the most important mechanical properties of a polymer and characterizes its flexibility. In 3D a formal definition of the persistence length is the length at which angular correlations in the tangent directions along the polymer are decreased on average by e times.[40] To estimate the persistence length of the BSA fibrils, we used three different calculation methods: bond correlation function (BCF), mean-squared end-to-end distance (MSED), and mean-squared midpoint displacement (MSMD) *versus* internal contour length l. Details of these methods can be found in the SI, with Figure S7 providing the graphical representation of each method. Persistence length estimation for flexible fibrils could be made by means of both end-to-end distance and bond correlation function without significant distortions (Figure 4A,C). However, for rigid fibrils only end-to-end distance and midpoint displacement methods provided acceptable
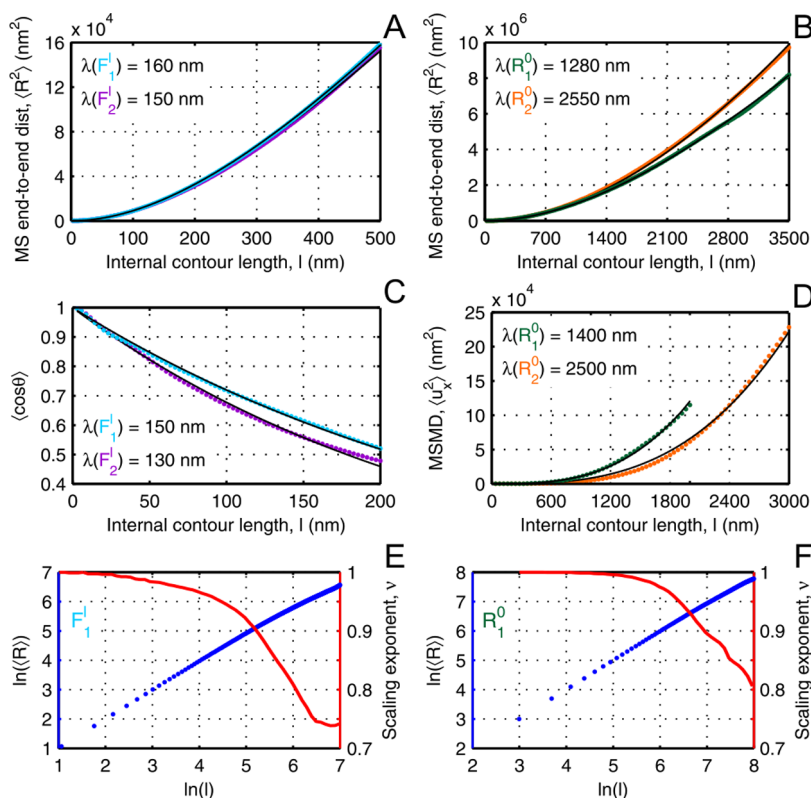
Figure 4. (A, B) Persistence length estimation for flexible and rigid fibrils by mean-squared end-to-end distance *versus* internal contour length fitted by eq S1. (C) Persistence length estimation by bond correlation function fitted by eq S2 for flexible fibrils. (D) Persistence length estimation by mean-squared midpoint displacement fitted by eq S3 for rigid fibrils. Resulting persistence length values are summarized in Table S2. Scaling exponent evolution for (E) thin flexible, type F_1^I, and (F) thin rigid, type R_1^0, fibrils, indicating that only F_1^I have reached the self-similar behavior of self-avoiding random walk in 2D.

accuracy (Figure 4B,D). All the fitting results for experimental data together with average lengths $\langle L \rangle$ and number of processed fibrils are given in Table S2.

The scaling exponent ν is a power term in the proportional dependence of the mean end-to-end distance *versus* internal contour length:[41] $\langle R \rangle \sim l^\nu$. When l is small ($l < \lambda$), the scaling exponent approaches 1, while for $l \gg \lambda$ the expected exponent for a self-avoiding random walk in 2D is 0.75. To extract the scaling exponent of the fibrils, we performed a linear fit of the natural logarithm of the end-to-end distance *versus* the natural logarithm of the contour length. A fit on the window from $\ln l - 0.25$ to $\ln l + 0.25$ yielded the scaling exponent at position $\ln l$. Figure 4E,F show the scaling exponent *versus* the natural logarithm of the internal contour length for two types of fibrils: flexible thin F_1^I and rigid thin without handedness R_1^0. Maximal fitting lengths at which statistics are significant enough to avoid graphic distortions for F_1^I fibrils and R_1^0 fibrils are $e^7 \cong 1097$ nm and $e^8 \cong 2981$ nm, respectively. Persistence lengths are $\cong 150$ nm for F_1^I fibrils and $\cong 1350$ nm for R_1^0 (Table S2). So, in the case of the flexible fibrils the fitting length is long enough ($\cong 5$ persistence lengths) to allow the scaling exponent to plateau and reach the stationary expected value of 0.75; in contrast, for the rigid fibrils the fitting length is

too short (2.2 persistence lengths) to allow the scaling exponent to attain a plateau, and its value remains above the asymptotic limit of 0.75. The attained plateau of ν for flexible fibrils indicates that chains have reached self-similarity and can be modeled using real chain statistics (self-avoiding random walk) in 2D.

Polymorphism in the BSA Fibrils and Relationship between Fibril Types. Further investigation reveals a sophisticated hierarchy in the BSA polymorphic fibril types and a complex relationship between them. A common pathway of structural polymorphic changes that is shared by a variety of fibrillated proteins and peptides is the transition of twisted ribbons to nanotubes with a transient intermediate state corresponding to helical ribbons.[42−44] We have found a similar transition pathway in the case of rigid BSA fibrils without periodicity. Only one flexible fibril is involved; hence we call it the single-fibril transformation pathway of BSA fibrillation. Figure 5A,B display evidence of polymorphic changes from F_1^I to R_1^0, as well as from F_2^I to R_2^0. The intermediate helical ribbon conformations are denoted as $[F_1^I]$ and $[F_2^I]$, respectively. Some rigid fibrils contain at one end a part corresponding to a flexible fibril in the helical ribbon conformation. Similar images of helical ribbon progression into nanotube were reported for enantiomeric-depsipeptide derivatives of
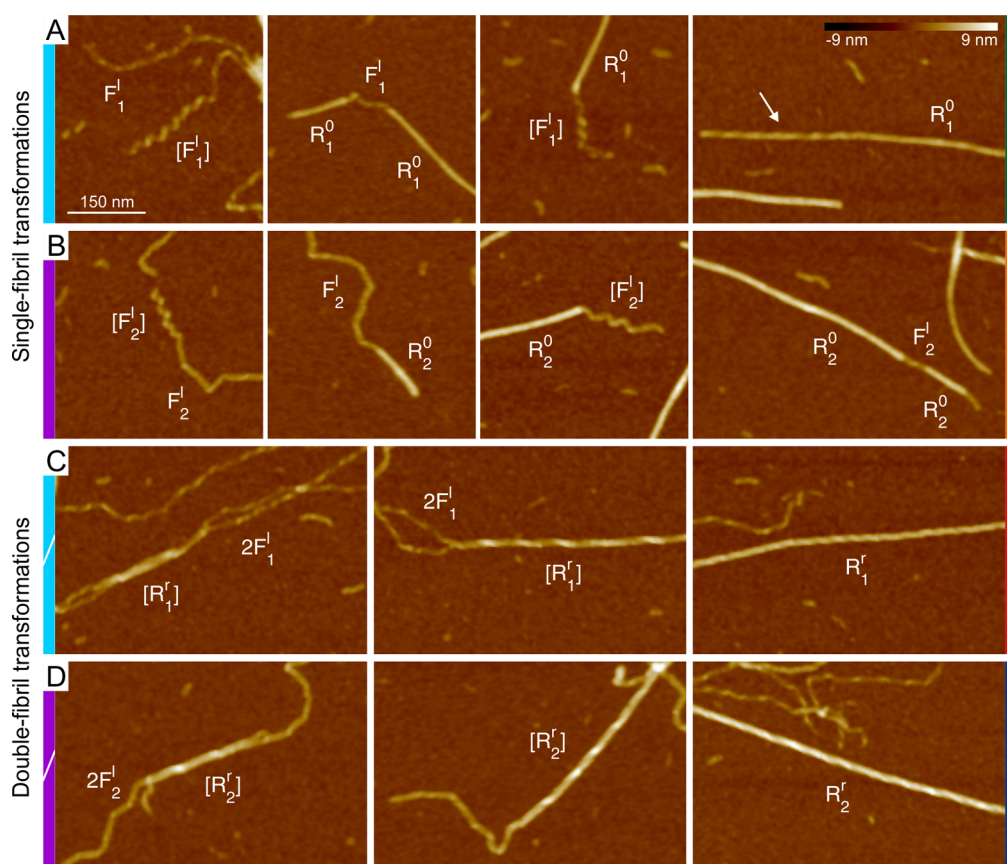
Figure 5. Pathways of the polymorphic transformations between (A) type F_1^l and R_1^0, (B) type F_2^l and R_2^0, (C) two fibrils of type F_1^l and R_1^r, and (D) two fibrils of type F_2^l and R_2^r. Intermediate forms of these transitions are identified with designations $[F_1^l]$, $[F_2^l]$, $[R_1^r]$, and $[R_2^r]$, respectively. In panel (A) a white arrow points to a place of R_1^0 where it is possible to observe a not yet fully closed region with a left-handed periodicity. In a single-fibril transformation only one mature flexible fibril evolves into another polymorphic type ($F^l \rightarrow [F^l] \rightarrow R^0$), while in the double-fibril transformation, two flexible fibrils of identical type form different periodical rigid fibrils of inverted handedness ($2F^l \rightarrow [R^r] \rightarrow R^r$). Scale bars apply to all images.

the amyloidogenic peptide amylin (20−29).[45] A white arrow in Figure 5A points to a place along the fibrils of the type R_1^0 where it is still possible to observe a not yet fully closed region with left-handed periodicity. This is additional evidence showing that single flexible BSA fibrils can transform into nanotubes *via* the sequence $F^l \rightarrow [F^l] \rightarrow R^0$.

The other two types of rigid fibrils are right-handed helical ribbons (Figure 2B) and follow an alternative pathway in their polymorphic evolution. Two left-handed flexible fibrils of the same type can wind together and form a new right-handed twisted ribbon with four protofilaments in cross-section (Figure 5C,D), denoted by $[R_1^r]$ or $[R_2^r]$, depending on the initial type of associating flexible fibrils. The last stage is the transformation to the helical right-handed ribbon R^r, so we call this pathway the double-fibril transformation pathway: $2F^l \rightarrow [R^r] \rightarrow R^r$. Thus BSA can self-assemble into various polymorphic states of amyloid fibrils with either handedness.

Discussion. The present results indicate that the globular protein BSA upon incubation at high temperature (90 °C) and in acidic environment (pH 2) can self-assemble into fibrillar structures with several

possible morphologies. In addition, the simultaneous coexistence of left- and right-handed amyloid fibrils is also resolved. Inversion on handedness with processing conditions has been reported before for bovine insulin fibrils upon vortexing[46] and upon changing the pH from 1.1 to 2.1,[47] but we are not aware of any work disclosing simultaneous coexistence of left- and right-handed fibrils from the same protein source. More importantly, a rationale is presented here for the switch of handedness, which goes beyond a previous understanding of macroscopic chirality as a result of the enantiomer precursors.[48]

The first step of the fibrillation process common to all possible pathways starts with the formation of single protofilaments, which can further assemble pairwise into double-stranded ribbons. The most stable conformation of these ribbons is a twisted configuration (characterized by a saddle-like curvature). However, kinetic energy or thermal fluctuations can promote occasional transition of twisted ribbons to the higher energetic status of helical ribbons (possessing a mean curvature). It is indeed now well understood that at low width to thickness ratio twisted ribbons are energetically favored, whereas after a critical width to thickness ratio, helical ribbons are energetically more
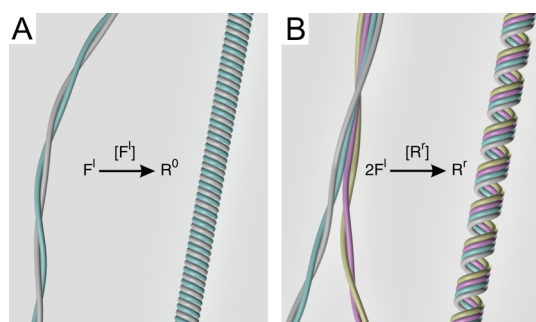
Figure 6. 3D schematic representations of the two main pathways in the BSA fibrillation process. (A) The single-fibril pathway occurs when the flexible left-handed twisted ribbons F^l transform into the rigid nanotube-like structure R^0. (B) The double-fibril pathway occurs when two left-handed twisted ribbons $2F^l$ wind together forming the rigid right-handed helical ribbon R^r.

stable.[42,44,49−52] Consistently, in two-stranded BSA fibrils, the twisted ribbons were prevalently observed in this work, while helical ribbons were detected only occasionally, inferring that the latter morphology is metastable at these conditions. The gap between edges in the helical ribbons can further vanish, driven by line tension energy reduction,[44] closing helical ribbons into nanotube-like fibrils. We detected only left-handed twisted and helical ribbons, which just prior to complete closure still maintain the same handedness. This can be systematically observed in transient helical ribbon conformations at the nanotube tails and, in extremely rare cases, along the nanotube contour prior to closure (Figure 5A, white arrow). Hence, flexible thin and thick left-handed twisted ribbons can undergo a polymorphic transformation into closed nanotubes *via* the helical ribbon transient state, as already reported by our group in other amyloid systems.[42−44] Most surprisingly, however, there is an alternative pathway to the formation of rigid fibrils. This takes place when two double-stranded flexible fibrils of the same type interact with each other, forming a ribbon with a doubled width and number of protofilaments (*i.e.*, four protofilaments). The widened ribbon preferred state now becomes a helical ribbon conformation, in agreement with expectations from the increased width to thickness ratio, but an additional interesting topological change also occurs: handedness switches from left-handed to right-handed. Interestingly enough, each of two flexible

types of fibrils F_1^l and F_2^l can follow this route to form rigid fibrils. The 3D reconstruction schemes of these fibril polymorphic pathways are illustrated in Figure 6. Thus, while single flexible fibrils F^l can form rigid thin nanotubes R^0 (Figure 6A) *via* an intermediate left-handed helical ribbon conformation [F^l], two flexible fibrils F^l can form one helical ribbon fibril with right-handed periodicity R^r, *via* a right-handed twisted ribbon [R^r] intermediate (Figure 6B). These results are supported by recent simulations suggesting that above a critical dihedral twisting angle of the constituting fibrils, handedness of the resulting fibril cluster can invert[53,54] if the assumption is made here that the initial two-stranded flexible fibrils F^l possess an intrinsic twist above this critical threshold.

CONCLUSIONS

A detailed statistical analysis of the topological features of BSA fibrils was carried out from their coordinates, tracked on high-resolution AFM images; at longer length scales, structural features of the fibrils were analyzed using a statistical polymer physics formalism. Six distinct polymorphic forms could be identified based on this study. Height profiles along the fibrils' contour length revealed the presence of either a periodicity with a well-defined pitch in some classes of fibrils (F_1^l, R_1^r, R_2^r), confirmed by fast Fourier transform analysis and autocorrelation function of height profiles, or undefined periodicity in other fibrils (F_2^l), or no periodicity in the remaining classes of fibrils (R_1^0, R_2^0). The persistence lengths of both flexible fibril types F_1^l and F_2^l were found to be close to each other. However, rigid thick fibrils R_2^0 and R_2^r have an average persistence length twice as much as rigid thin fibrils R_1^0 and R_1^r. When the thin fibrils grow to a long-enough contour length (≫the persistence length), they follow a classical self-avoiding random walk in two dimensions with a fractal exponent of 3/4; in contrast, in rigid fibrils the persistence length is too large (or, equivalently the contour length is too short) to reach self-similarity scaling behavior. On the basis of this analysis, the interdependence between the different polymorphic states was conclusively resolved, in terms of structure, composition, and handedness. This work provides the first compelling evidence that inversion of handedness during globular protein fibrillation is accompanied by an increasing level of structural complexity.

MATERIALS AND METHODS

BSA Fibril Formation. Prior to the incubation process, BSA (Sigma-Aldrich, product no. A7030, lyophilized powder ≥98%) was dialyzed with a semipermeable membrane (Spectra/Por dialysis membrane 1, MWCO 6−8 kDa) for 3 days. Fibrils were obtained by dissolving 1.5 g of the protein in 23.5 mL of Milli-Q water adjusted to pH 2 with HCl. A vessel containing the resulting 6 w/w % protein solution was kept in an oil bath at

high temperature (90 °C) for more than 6 days (145 h). To follow the fibrillation kinetics, small aliquots were taken, specifically at 0.5, 1, 2, 3, 4, 5, 6, 20, 40, 70, 100, and 145 h, and immediately placed in an ice−water cooling bath to quench the growth kinetics. Mild agitation was applied throughout the whole incubation process.

Atomic Force Microscopy. The samples taken at different incubation times were diluted to a BSA concentration 0.1 w/w %

with pH 2 Milli-Q water. Then 20 μL aliquots of diluted solution were deposited onto freshly cleaved mica substrates. After a 2 min equilibration each sample was rinsed with 1 mL of Milli-Q water and gently dried with an air flow. AFM scanning was performed with a MultiMode VIII scanning probe microscope (Bruker, USA) operated in a tapping mode under ambient conditions and with cantilevers having a nominal vibrating frequency of 150 kHz.

Fibril Tracking. In order to apply statistical analysis to the fibril systems, we obtained their coordinates using an in-house program written in MATLAB. Each tracked fibril in the AFM image is identified as a contour, a sequence of points ordered along the fibril's middle line from one end to the other. Hence, the position of any fibril can be determined by a set of coordinates of all points that the fibril's contour incorporates. All contours have a constant distance between the point's projections on the XY plane, the step size s, which has a typical value on the order of the pixel size of the AFM image. The initial position of each contour is assigned manually with auxiliary help from the A* pathfinding algorithm.[55] To obtain subpixel accuracy, contours were deformed and fitted precisely to a bright ridge of a fiber using an Open Active Contours algorithm,[56,57] slightly adjusted for our purposes. All traced fibril data were extracted from high-resolution AFM images with metrical dimensions 15 × 15 μm and resolution 5120 × 5120 pixels. Images of the 40 h sample were used for tracking flexible classes of fibrils, while data on rigid fibrils were obtained from AFM images of the 100 h sample. Data on rigid fibrils from images acquired with a large AFM scanner (100 × 100 μm edge size and analogous resolution) were used for persistence length and scaling exponent determination. In this procedure, the fibrils that cross the image edge were eliminated from the statistics to reduce errors in contour length estimation. In total, 4035 fibrils were tracked in this study to reach sufficient statistical significance. The entire data processing and statistical analysis were performed using the same in-house software.

Conflict of Interest: The authors declare no competing financial interest.

Supporting Information Available: Supplemental Figure 1, SDS-PAGE analysis; Supplemental Figure 2, CD measurements of the filtered BSA samples; Supplemental Figure 3, AFM image of the BSA fibrils' massive aggregate; Supplemental Figure 4, AFM images of single protofilaments; Supplemental Figure 5, height distributions among all contours' height values; Supplemental Figure 6, pitch size estimation for the type R_2^r; Supplemental Figure 7, persistence length calculation methods. Supplemental Table 1, summary of the fibril height values analysis; Supplemental Table 2, persistence lengths of the fibril types. This material is available free of charge *via* the Internet at http://pubs.acs.org.

REFERENCES AND NOTES

1. Whitesides, G. M.; Mathias, J. P.; Seto, C. T. Molecular Self-Assembly and Nanochemistry: A Chemical Strategy for the Synthesis of Nanostructures. *Science* **1991**, *254*, 1312–1319.
2. Zhang, S. Emerging Biological Materials through Molecular Self-Assembly. *Biotechnol. Adv.* **2002**, *20*, 312–339.
3. Mezzenga, R.; Fischer, P. The Self-Assembly, Aggregation and Phase Transitions of Food Protein Systems in One, Two and Three Dimensions. *Rep. Prog. Phys.* **2013**, *76*, 046601.
4. Fändrich, M. On the Structural Definition of Amyloid Fibrils and Other Polypeptide Aggregates. *Cell. Mol. Life Sci.* **2007**, *64*, 2066–2078.
5. Marshall, K. E.; Serpell, L. C. Structural Integrity of β-Sheet Assembly. *Biochem. Soc. Trans.* **2009**, *37*, 671–676.
6. Mondal, M.; Trivedy, K.; Kumar, S. N. The Silk Proteins, Sericin and Fibroin in Silkworm, Bombyx Mori Linn. - A Review. *Caspian J. Environ. Sci.* **2007**, *5*, 63–76.
7. Irvine, G. B.; El-Agnaf, O. M.; Shankar, G. M.; Walsh, D. M. Protein Aggregation in the Brain: The Molecular Basis for Alzheimer's and Parkinson's Diseases. *Mol. Med.* **2008**, *14*, 451–464.
8. Lashuel, H. A.; Lansbury, P. T. J. Are Amyloid Diseases Caused by Protein Aggregates Thatmimic Bacterial Pore-Forming Toxins? *Q. Rev. Biophys.* **2006**, *39*, 167–201.
9. Selkoe, D. J. Folding Proteins in Fatal Ways. *Nature* **2003**, *426*, 900–904.
10. Dobson, C. M. Protein Folding and Misfolding. *Nature* **2003**, *426*, 884–890.
11. Chiti, F.; Dobson, C. M. Protein Misfolding, Functional Amyloid, and Human Disease. *Annu. Rev. Biochem.* **2006**, *75*, 333–366.
12. Bolder, S. G.; Hendrickx, H.; Sagis, L. M. C.; van der Linden, E. Fibril Assemblies in Aqueous Whey Protein Mixtures. *J. Agric. Food Chem.* **2006**, *54*, 4229–4234.
13. Goers, J.; Permyakov, S. E.; Permyakov, E. A.; Uversky, V. N.; Fink, A. L. Conformational Prerequisites for α-Lactalbumin Fibrillation. *Biochemistry* **2002**, *41*, 12546–12551.
14. Adamcik, J.; Jung, J.-M.; Flakowski, J.; De Los Rios, P.; Dietler, G.; Mezzenga, R. Understanding Amyloid Aggregation by Statistical Analysis of Atomic Force Microscopy Images. *Nat. Nanotechnol.* **2010**, *5*, 423–428.
15. Arnaudov, L. N.; de Vries, R. Strong Impact of Ionic Strength on the Kinetics of Fibrilar Aggregation of Bovine β-Lactoglobulin. *Biomacromolecules* **2006**, *7*, 3490–3498.
16. Loveday, S. M.; Wang, X. L.; Rao, M. A.; Anema, S. G.; Singh, H. β-Lactoglobulin Nanofibrils: Effect of Temperature on Fibril Formation Kinetics Fibril Morphology and the Rheological Properties of Fibril Dispersions. *Food Hydrocolloids* **2012**, *27*, 242–249.
17. Lara, C.; Gourdin-Bertin, S.; Adamcik, J.; Bolisetty, S.; Mezzenga, R. Self-Assembly of Ovalbumin into Amyloid and Non-Amyloid Fibrils. *Biomacromolecules* **2012**, *13*, 4213–4221.
18. Veerman, C.; de Schiffart, G.; Sagis, L. M. C.; van der Linden, E. Irreversible Self-Assembly of Ovalbumin into Fibrils and the Resulting Network Rheology. *Int. J. Biol. Macromol.* **2003**, *33*, 121–127.
19. Lara, C.; Usov, I.; Adamcik, J.; Mezzenga, R. Sub-Persistence-Length Complex Scaling Behavior in Lysozyme Amyloid Fibrils. *Phys. Rev. Lett.* **2011**, *107*, 238101.
20. Frare, E.; Polverino De Laureto, P.; Zurdo, J.; Dobson, C. M.; Fontana, A. A Highly Amyloidogenic Region of Hen Lysozyme. *J. Mol. Biol.* **2004**, *340*, 1153–1165.
21. Arnaudov, L. N.; de Vries, R. Thermally Induced Fibrillar Aggregation of Hen Egg White Lysozyme. *Biophys. J.* **2005**, *88*, 515–526.
22. Pearce, F. G.; Mackintosh, S. H.; Gerrard, J. A. Formation of Amyloid-Like Fibrils by Ovalbumin and Related Proteins under Conditions Relevant to Food Processing. *J. Agric. Food. Chem.* **2007**, *55*, 318–322.
23. Mezzenga, R.; Schurtenberger, P.; Burbidge, A.; Michel, M. Understanding Foods as Soft Materials. *Nat. Mater.* **2005**, *4*, 729–740.
24. Nicolai, T.; Britten, M.; Schmitt, C. β-Lactoglobulin and WPI Aggregates: Formation, Structure and Applications. *Food Hydrocolloids* **2011**, *25*, 1945–1962.
25. Mankar, S.; Anoop, A.; Sen, S.; Maji, S. K. Nanomaterials: Amyloids Reflect Their Brighter Side. *Nano Rev.* **2011**, *2*, 6032.
26. Knowles, T. P.; Buehler, M. J. Nanomechanics of Functional and Pathological Amyloid Materials. *Nat. Nanotechnol.* **2011**, *6*, 469–479.
27. Li, C.; Adamcik, J.; Mezzenga, R. Biodegradable nanocomposites of amyloid fibrils and graphene with shape-memory and enzyme-sensing properties. *Nat. Nanotechnol.* **2012**, *7*, 421–427.
28. Holm, N. K.; Jespersen, S. K.; Thomassen, L. V.; Wolff, T. Y.; Sehgal, P.; Thomsen, L. A.; Christiansen, G.; Andersen, C. B.; Knudsen, A. D.; Otzen, D. E. Aggregation and Fibrillation of Bovine Serum Albumin. *Biochim. Biophys. Acta* **2007**, *1774*, 1128–1138.
29. Bramanti, E.; Ferrari, C.; Angeli, V.; Onor, M.; Synovec, R. E. Characterization of BSA Unfolding and Aggregation Using

a Single-Capillary Viscometer and Dynamic Surface Tension Detector. *Talanta* **2011**, *85*, 2553–2561.

30. Veerman, C.; Sagis, L. M. C.; Heck, J.; van der Linden, E. Mesostructure of Fibrillar Bovine Serum Albumin Gels. *Int. J. Biol. Macromol.* **2003**, *31*, 139–146.

31. Murayama, K.; Tomida, M. Heat-Induced Secondary Structure and Conformation Change of Bovine Serum Albumin Investigated by Fourier Transform Infrared Spectroscopy. *Biochemistry* **2004**, *43*, 11526–11532.

32. Bhattacharya, M.; Jain, N.; Mukhopadhyay, S. Insights into the Mechanism of Aggregation and Fibril Formation from Bovine Serum Albumin. *J. Phys. Chem. B* **2011**, *115*, 4195–4205.

33. Su, R.; Qi, W.; He, Z.; Zhang, Y.; Jin, F. Multilevel Structural Nature and Interactions of Bovine Serum Albumin during Heat-Induced Aggregation Process. *Food Hydrocolloids* **2008**, *22*, 995–1005.

34. Vetri, V.; D'Amico, M.; Foderà, V.; Leone, M.; Ponzoni, A.; Sberveglieri, G.; Militello, V. Bovine Serum Albumin Protofibril-Like Aggregates Formation: Solo but Not Simple Mechanism. *Arch. Biochem. Biophys.* **2011**, *508*, 13–24.

35. Jordens, S.; Adamcik, J.; Amar-Yuli, I.; Mezzenga, R. Disassembly and Reassembly of Amyloid Fibrils in Water-Ethanol Mixtures. *Biomacromolecules* **2011**, *12*, 187–193.

36. Adamcik, J.; Mezzenga, R. Study of Amyloid Fibrils via Atomic Force Microscopy. *Curr. Opin. Colloid Interface Sci.* **2012**, *17*, 369–376.

37. Zhang, S.; Andreasen, M.; Nielsen, J. T.; Liu, L.; Nielsen, E. H.; Song, J.; Ji, G.; Sun, F.; Skrydstrup, T.; Besenbacher, F.; *et al*. Coexistence of Ribbon and Helical Fibrils Originating from hIAPP20-29 Revealed by Quantitative Nanomechanical Atomic Force Microscopy. *Proc. Natl. Acad. Sci. U.S.A.* **2013**, *110*, 2798–2803.

38. Lara, C.; Adamcik, J.; Jordens, S.; Mezzenga, R. General Self-Assembly Mechanism Converting Hydrolyzed Globular Proteins into Giant Multistranded Amyloid Ribbons. *Biomacromolecules* **2011**, *12*, 1868–1875.

39. Meinhardt, J.; Sachse, C.; Hortschansky, P.; Grigorieff, N.; Fändrich, M. Aβ(1−40) Fibril Polymorphism Implies Diverse Interaction Patterns in Amyloid Fibrils. *J. Mol. Biol.* **2009**, *386*, 869–877.

40. Rubinstein, M.; Colby, R. H. *Polymer Physics*; Oxford University Press, 2003; pp 54−60.

41. de Gennes, P. G. *Scaling Concepts in Polymer Physics*; Cornell University Press, 1979; pp 43−46.

42. Adamcik, J.; Castelletto, V.; Bolisetty, S.; Hamley, I. W.; Mezzenga, R. Direct Observation of Time-Resolved Polymorphic States in the Self-Assembly of End-Capped Heptapeptides. *Angew. Chem., Int. Ed.* **2011**, *50*, 5495–5498.

43. Adamcik, J.; Mezzenga, R. Proteins Fibrils from a Polymer Physics Perspective. *Macromolecules* **2012**, *45*, 1137–1150.

44. Lara, C.; Handschin, S.; Mezzenga, R. Towards Lysozyme Nanotube and 3D Hybrid Self-Assembly. *Nanoscale* **2013**, *5*, 7197–7201.

45. Elgersma, R. C.; Mulder, G. E.; Posthuma, G.; Rijkers, D. T. S.; Liskamp, R. M. J. Mirror image supramolecular helical tapes formed by the enantiomeric-depsipeptide derivatives of the amyloidogenic peptide amylin(20−29). *Tetrahedron Lett.* **2008**, *49*, 987–991.

46. Dzwolak, W.; Loksztejn, A.; Galinska-Rakoczy, A.; Adachi, R.; Goto, Y.; Rupnicki, L. Conformational Indeterminism in Protein Misfolding: Chiral Amplification on Amyloidogenic Pathway of Insulin. *J. Am. Chem. Soc.* **2007**, *129*, 7517–7522.

47. Kurouski, D.; Dukor, R. K.; Lu, X.; Nafie, L. A.; Lednev, I. K. Normal and Reversed Supramolecular Chirality of Insulin Fibrils Probed by Vibrational Circular Dichroism at the Protofilament Level of Fibril Structure. *Biophys. J.* **2012**, *103*, 522–531.

48. Rubin, N.; Perugia, E.; Goldschmidt, M.; Fridkin, M.; Addadi, L. Chirality of Amyloid Suprastructures. *J. Am. Chem. Soc.* **2008**, *130*, 4602–4603.

49. Oda, R.; Huc, I.; Schmutz, M.; Candau, S. J.; MacKintosh, F. C. Tuning bilayer twist using chiral counterions. *Nature* **1999**, *399*, 566–569.

50. Sawa, Y.; Ye, F.; Urayama, K.; Takigawa, T.; Gimenez-Pinto, V.; Selinger, R. L. B.; Selinger, J. V. Shape Selection of Twist-Nematic-Elastomer Ribbons. *Proc. Natl. Acad. Sci. U.S.A.* **2011**, *108*, 6364–6368.

51. Teresi, L.; Varano, V. Modeling Helicoid to Spiral-Ribbon Transitions of Twist-Nematic Elastomers. *Soft Matter* **2013**, *9*, 3081–3088.

52. Ziserman, L.; Lee, H. Y.; Raghavan, S. R.; Mor, A.; Danino, D. Unraveling the Mechanism of Nanotube Formation by Chiral Self-Assembly of Amphiphiles. *J. Am. Chem. Soc.* **2011**, *133*, 2511–2517.

53. Olesen, S. W.; Fejer, S. N.; Chakrabarti, D.; Wales, D. J. A Left-Handed Building Block Self-Assembles into Rightand Left-Handed Helices. *RSC Adv.* **2013**, *3*, 12905–12908.

54. Gruziel, M.; Dzwolak, W.; Szymczak, P. Chirality Inversions in Self-Assembly of Fibrillar Superstructures: A Computational Study. *Soft Matter* **2013**, *9*, 8005–8013.

55. Hart, P. E.; Nilsson, N. J.; Raphael, B. A. A Formal Basis for the Heuristic Determination of Minimal Cost Paths. *IEEE Trans. Syst. Sci. Cybern.* **1968**, *ssc-4*, 100−107.

56. Kass, M.; Witkin, A.; Terzopoulos, D. Snakes: Active Contour Models. *Int. J. Comput. Vision* **1988**, 321–331.

57. Smith, M. B.; Li, H.; Shen, T.; Huang, X.; Yusuf, E.; Vavylonis, D. Segmentation and Tracking of Cytoskeletal Filaments Using Open Active Contours. *Cytoskeleton* **2010**, *67*, 693–705.